Elastic consequences of a single plastic event : towards a realistic account of structural disorder and shear wave propagation in models of flowing amorphous solids

Email address: alexandre.nicolas@ujf-grenoble.fr (Alexandre NICOLAS)

Preprint submitted to Journal of the Mechanics and Physics of Solids February 16, 2015

Elastic consequences of a single plastic event : towards a realistic account of structural disorder and shear wave propagation in models of flowing amorphous solids

Alexandre NICOLAS[a,b], Francesco PUOSI[a,b], Hideyuki MIZUNO[a,b,1], Jean-Louis BARRAT[a,b,c]

[a] *Univ. Grenoble Alpes, LIPhy, F-38000 Grenoble, France*
[b] *CNRS, LIPhy, F-38000 Grenoble, France*
[c] *Institut Laue-Langevin, 6 rue Jules Horowitz, BP 156, F-38042 Grenoble, France*

Abstract

Shear transformations (*i.e.*, localised rearrangements of particles resulting in the shear deformation of a small region of the sample) are the building blocks of mesoscale models for the flow of disordered solids. In order to compute the time-dependent response of the solid material to such a shear transformation, with a proper account of elastic heterogeneity and shear wave propagation, we propose and implement a very simple Finite-Element (FE) - based method. Molecular Dynamics (MD) simulations of a binary Lennard-Jones glass are used as a benchmark for comparison, and information about the microscopic viscosity and the local elastic constants is directly extracted from the MD system and used as input in FE. We find very good agreement between FE and MD regarding the temporal evolution of the *disorder-averaged* displacement field induced by a shear transformation, which turns out to coincide with the response of a *uniform* elastic medium. However, *fluctuations* are relatively large, and their magnitude is satisfactorily captured by the FE simulations of an elastically heterogeneous system. Besides, accounting for elastic anisotropy on the mesoscale is not crucial in this respect.

The proposed method thus paves the way for models of the rheology of amorphous solids which are both computationally efficient and realistic, in that structural disorder and inertial effects are accounted for.

Keywords: shear transformation, plastic event, structural disorder, elastic moduli
PACS: 62.20.D-, 83.80.Ab, 02.70.Dh, 61.43.Bn

1. Introduction

Glasses are macroscopically isotropic and homogeneous. Microscopically, the absence (or elusiveness) of a clear structural signature of the liquid-to-

Email address: alexandre.nicolas@ujf-grenoble.fr (Alexandre NICOLAS)

1. Present address : German Aerospace Center (DLR), Institute of Materials Physics in Space, Linder Höhe, 51147 Köln

glass transition upon cooling may fallaciously lead one to believe that the property of structural homogeneity holds down to the microscale in glasses, as it does in liquids. In the past decades, it has become clear that this idea is completely erroneous : structural disorder is often regarded as a crucial aspect not only of the glass transition, but also of the flow of soft or hard glassy materials, and more generally amorphous solids, such as emulsions, foams, dense gels, and granular matter. For instance, several theories of the glass transition, including the Random First Order Theory (Lubchenko and Wolynes, 2007; Berthier and Biroli, 2011) and kinetically constrained models with facilitated dynamics (Chandler and Garrahan, 2010), put the focus on dynamical heterogeneities, that is, the coexistence of regions with fast and slow (arrested) dynamics.

Heterogeneities are even more manifest when the materials are forced to flow. Instead of a homogeneous deformation, one observes localised bursts of particle rearrangements, called shear transformations or plastic events, embedded in an essentially elastically deforming medium (Argon and Kuo, 1979; Falk and Langer, 1998; Schall et al., 2007; Amon et al., 2012). These irreversibly rearranging regions coincide with "weak" zones where the local elastic (shear) moduli vanish at the onset of a plastic event (Tsamados et al., 2009). By simply looking at the instantaneous (static) configuration of the system, computing its soft modes, and observing where they concentrate, one can predict statistically (but only to a *limited* extent) the position of future rearrangements (Widmer-Cooper et al., 2008; Rottler et al., 2014). Not only does microscopic structural disorder play the leading role in fixing where the rearrangements will occur, but it also affects the way stress is redistributed in the medium during these plastic events, *i.e.*, the propagation of the shear waves originating from the rearranging region.

This stress redistribution is generally described as the solution of an Eshelby inclusion problem in a uniform linear elastic medium (Eshelby, 1957), with an inclusion that is often assumed pointwise in lattice-based rheological models, for convenience (Picard et al., 2004, 2005; Vandembroucq and Roux, 2011; Talamali et al., 2011; Lin et al., 2014; Martens et al., 2011, 2012; Nicolas et al., 2014a). The solution is given by an elastic propagator $\mathcal{G}$ with a characteristic four-fold angular symmetry and an r^{-2} spatial decay in two dimensions, in line with experiments on, *e.g.*, dense emulsions (Desmond and Weeks, 2013) (also see Budrikis and Zapperi (2013); Sandfeld et al. (2015) for a discussion on this elastic propagator and its possible numerical implementations). However, some of us very recently showed that such description only holds *on average* (Puosi et al., 2014) ; if an individual plastic event is considered, the description is unreliable, because the average response is blurred by sample-to-sample fluctuations, presumably associated with the elastic heterogeneity of the material. Moreover, this approach neglects inertial effects by supposing instantaneous mechanical equilibration, or, in other words, an infinite shear wave velocity, whereas the role of inertia on the statistics of avalanche sizes has been numerically evidenced (Salerno et al., 2012; Salerno and Robbins, 2013). These two deficiencies, possibly among others, undermined a recent endeavour of ours to reproduce the spatio-temporal correlations in the flow of a disordered solid with a coarse-grained model using the

elastic propagator $\mathcal{G}$ (Nicolas et al., 2014b).

The objective of this contribution is to go beyond the average, equilibrium-based description in terms of the elastic propagator; we aim to devise and put to the test a *minimal framework* allowing to capture the fluctuations in the response due to structural disorder, as well as the propagation of the shear waves, in two dimensions (2D). To this end, we implement a basic Finite Element (FE) code and use Molecular Dynamics (MD) simulations of an athermal solid as a benchmark. In so doing, we show how the microscopic data about, *e.g.*, the local elastic constants can be extracted from the MD system and used as input in FE.

In Section 2, we present the MD simulation method and we introduce our simplified FE algorithm. Section 3 is concerned with the fitting of the mechanical parameters required by FE, in particular, the calculation of the local elastic constants of the MD solid. Section 4 clarifies the protocol to trigger artificial shear transformations. Finally, Sections 5, 6, and 7 describe the disorder-averaged elastic response to this localised transformation, the fluctuations around this average, and the response in a particular configuration of the system, respectively.

2. Methods

2.1. Molecular Dynamics

To probe the flow properties of amorphous solids, we resort to MD simulations of a 2D amorphous system. More precisely, we simulate a binary mixture of A and B particles, with $N_A = 32500$ and $N_B = 17500$, of respective diameters $\sigma_{AA} = 1.0$ and $\sigma_{BB} = 0.88$, confined in a square box of dimensions $205\sigma_{AA} \times 205\sigma_{AA}$, with periodic boundary conditions. The system is at reduced density 1.2. The particles, of mass $m = 1$, interact via a pairwise Lennard-Jones potential,

$$V_{\alpha\beta}(r) = 4\epsilon_{\alpha\beta}\left[\left(\frac{\sigma_{\alpha\beta}}{r}\right)^{12} - \left(\frac{\sigma_{\alpha\beta}}{r}\right)^{6}\right],$$

where $\alpha, \beta = A, B$, $\sigma_{AB} = 0.8$,$\epsilon_{AA} = 1.0$, $\epsilon_{AB} = 1.5$, and $\epsilon_{BB} = 0.5$. The potential is truncated at $r_c = 2.5\sigma_{AA}$ and shifted for continuity.

We conduct our study in the athermal limit, by thermostatting the system to zero temperature, so that no fluctuating force appears in the equations of motion, *viz.*,

$$\begin{aligned} \frac{d\boldsymbol{r_i}}{dt} &= \boldsymbol{v_i} \\ m\frac{d\boldsymbol{v_i}}{dt} &= -\sum_{i\neq j}\frac{\partial V(r_{ij})}{\partial \boldsymbol{r_{ij}}} + \boldsymbol{f_i}^D. \end{aligned} \tag{1}$$

The dissipative force $\boldsymbol{f_i}^D$ experienced by particle i is computed with a Dissipative Particle Dynamics (DPD) scheme, whereby particles are damped on the basis of their relative velocities with respect to their neighbours. More

precisely, ${\boldsymbol{f_i}}^D$ reads

$$
\begin{aligned}
{\boldsymbol{f_i}}^D &= -\sum_{j\neq i} \zeta w^2\left(r_{ij}\right) \frac{\boldsymbol{v_{ij}}\cdot\boldsymbol{r_{ij}}}{r_{ij}^2}\boldsymbol{r_{ij}} \qquad (2)\\
\text{where } w(r) &\equiv \begin{cases} 1-\frac{r}{r_c} & \text{if } r<r_c,\\ 0 & \text{otherwise.}\end{cases}
\end{aligned}
$$

Here, $\boldsymbol{v_{ij}}\equiv\boldsymbol{v_i}-\boldsymbol{v_j}$ denotes the relative velocity of particle i with respect to j, the vector $\boldsymbol{r_{ij}}\equiv\boldsymbol{r_i}-\boldsymbol{r_j}$ connects particle j to i, the cut-off distance is set to $r_c=2.5\sigma_{AA}$, and ζ controls the damping intensity. Different values of ζ will be tested to probe the different damping regimes, from underdamped ($\zeta\lesssim 1$) to highly overdamped ($\zeta\gg 1$). Note that, in Eq. 2, the projection of the force onto the radial vector $\boldsymbol{r_{ij}}$ is required in order to conserve angular momentum. Several other virtues of DPD have been exposed by Soddemann et al. (2003). As far as we are concerned, one of the main advantages is that, in the light of the recent work of Varnik et al. (2014), experimentally measured correlations in the flow of amorphous solids are better reproduced numerically when dissipation is based on *relative* particle velocities, in opposition to a mean-field damping scheme, in which *absolute* velocities (with respect to a hypothetic solvent flow) are used. The impact of this implementation on the propagation of shear waves will be discussed in Section 5.2.

However, the DPD algorithm does not conserve the position of the centre of mass of the system *a priori*. Since the ensuing global translations of the system may disturb the forthcoming analysis of displacements in reponse to shear transformations, the system is regularly re-centred during the simulation.

Equations 1 are integrated with the velocity Verlet algorithm with $\delta t = 0.005$. In all the following, we use $\tau_{LJ}\equiv\sqrt{m\sigma_{AA}^2/\epsilon}$ as the unit of time and σ_{AA} as the unit of length.

2.2. Simplified Finite Elements

In the presence of elastic heterogeneities, the elastic response to a localised shear transformation becomes intractable to analytical calculations. This notably implies that the Fast Fourier Transform routine commonly used in elastoplastic models needs to be replaced. As a minimal substitute, we propose a simplified FE algorithm, which will also allow us to account for inertial effects.

The FE method consists in discretising a Continuum Mechanics equation onto a mesh. Here, the Continuum Mechanics equation involves elastic and dissipative (viscous) forces, as well as inertia ; hence, the momentum conservation equation reads

$$
\underbrace{\rho\frac{D\dot{\boldsymbol{u}}}{Dt}(\boldsymbol{r},t)}_{\text{inertial force}} = \underbrace{\nabla\cdot[\mathbf{C}(\boldsymbol{r},t)\boldsymbol{\epsilon}(\boldsymbol{r},t)]}_{\text{elasticity}} + \underbrace{\eta\nabla^2\dot{\boldsymbol{u}}(\boldsymbol{r},t)}_{\text{viscosity}}, \qquad (3)
$$

where $\boldsymbol{u}$ and $\boldsymbol{\epsilon}$ are the displacement and strain fields, respectively, ${}^{D\bullet}/_{Dt}\equiv {}^{\partial\bullet}/_{\partial t}+(\boldsymbol{v}\cdot\nabla)\bullet$ denotes the convected derivative, dots denote time derivatives,

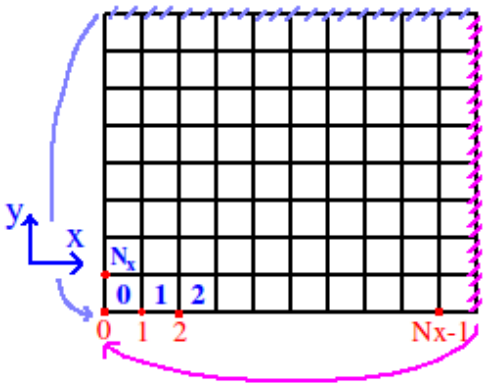

Figure 1: Sketch of the FE mesh. The system is periodic in both directions, so that column N_x coincides with column 0 and row N_y coincides with row 0. There are $N = N_x \times N_y$ nodes and elements.

ρ is the (area) density of the material, $\mathbf{C}$ denotes a local stiffness matrix, and η is the microscopic viscosity. Upon discretisation, it turns into

$$\underbrace{\boldsymbol{\mathcal{M}} \cdot \ddot{u}}_{\text{inertial force}} = \underbrace{\boldsymbol{\mathcal{K}} \cdot u}_{\text{elasticity}} + \underbrace{\boldsymbol{\mathcal{H}} \cdot \dot{u}}_{\text{viscosity}}, \tag{4}$$

where u is now a shorthand for the high-dimensional vector

$$\left(\; u_x^{(\mathbf{N-1})}, \quad u_y^{(\mathbf{N-1})}, \quad \ldots \quad u_x^{(\mathbf{0})}, \quad u_y^{(\mathbf{0})} \; \right)^\top$$

containing the displacements along x and y at the N nodes of the mesh. $\boldsymbol{\mathcal{M}}$, $\boldsymbol{\mathcal{K}}$, and $\boldsymbol{\mathcal{H}}$ are $2N \times 2N$ real matrices (to be specified later), and the dependences on time have been omitted.

Bearing in mind our pursuit of minimalism, we choose a simple (static) regular square meshgrid, as sketched in Fig. 1. In an element, the local strain $\boldsymbol{\epsilon} \equiv \left(\; \epsilon_{xx}, \quad \epsilon_{yy}, \quad \sqrt{2}\epsilon_{xy} \; \right)^\top$, using condensed notations for 2D symmetric tensors, is a function of the displacements at the local nodes, and we make the approximation of a *uniform* strain within each element [2]. For convenience, let us number these nodes from 0 to 3 counter-clockwise, for a given element, starting from the bottom left corner, *viz.*, ${}^{3}_{0}\square^{2}_{1}$. In an analogous way, the (uniform) elemental stress $\boldsymbol{\sigma}^{\text{el}}$ is derived from the nodal forces $\left(f_x^{\text{el}}, f_y^{\text{el}}\right)$. Since the mesh is regular, we can define a constant 3×8 real matrix $\mathbf{B}$ that relates, in a given element, the (nodal) displacements to the (elemental) strains, on the one hand, and the (nodal) forces to the (elemental) stresses, on the other hand, *viz.*,

2. In practice, our simplified FE method is therefore close to a Finite Volume method.

$$\begin{pmatrix} \epsilon_{xx} \\ \epsilon_{yy} \\ \sqrt{2}\epsilon_{xy} \end{pmatrix} = \mathbf{B} \cdot \begin{pmatrix} u_x^{(0)} \\ u_y^{(0)} \\ \vdots \\ u_x^{(3)} \\ u_y^{(3)} \end{pmatrix} \text{ and } \begin{pmatrix} \sigma_{xx}^{\mathrm{el}} \\ \sigma_{yy}^{\mathrm{el}} \\ \sqrt{2}\sigma_{xy}^{\mathrm{el}} \end{pmatrix} = -\mathbf{B} \cdot \begin{pmatrix} f_x^{\mathrm{el}\,(0)} \\ f_y^{\mathrm{el}\,(0)} \\ \vdots \\ f_x^{\mathrm{el}\,(3)} \\ f_y^{\mathrm{el}\,(3)} \end{pmatrix}. \quad (5)$$

The expression of the matrix $\mathbf{B}$ is given in AppendixA, along with further details pertaining to the implementation of the FE routine and the computation of the matrices $\boldsymbol{\mathcal{M}}$, $\boldsymbol{\mathcal{K}}$, and $\boldsymbol{\mathcal{H}}$ appearing in Eq. 4. Note that the $\sqrt{2}$ prefactors have been introduced with foresight (see Section 3.2) and the "minus" sign preceding $\mathbf{B}$ in Eq. A.1 is due to the fact that $\boldsymbol{f}^{\mathrm{el}\,(i)}$ is the force exerted *by* the element *on* node i.

The resulting routine is still simple enough to be used quite efficiently in a coarse-grained model. In particular, (see AppendixA.4), the global force-displacement matrix is constant and, accordingly, only has to be inverted *once*, at the beginning of the simulation.

On the other hand, there are naturally a few downsides to this simplicity. First and foremost, it is only marginally stable, insofar as the convergence of the discrete FE solution to the continuous solution of Eq. 3 is not guaranteed when the mesh size tends to zero. Consequently, this scheme is not suited to general purpose. However, as will be shown below, it is both satisfactory and very convenient for the modelling of (the response to) shear transformations, where elements represent material regions of finite size. In particular, the frequently encountered checkerboard issue, whereby high and low displacements/velocities alternate erratically in neighbouring cells (hence the image of a checkerboard), is practically circumvented, provided that shear transformations span four adjacent elements (a "macro-element") and inertia is present, *i.e.*, $\rho \neq 0$.

3. Fitting of elastic and viscous parameters

We are now left with the task of fitting the physical parameters appearing in Eq. 3 with the MD parameters. Neglecting mesoscopic density fluctuations, the density ρ and the miscroscopic viscosity η are supposed to be constant, while the stiffness matrix $\mathbf{C}(\boldsymbol{r},t)$ is allowed to vary in space.

3.1. Viscosity

To fit the viscosity η in Eq. 3, we compare the stress due to homogeneous shear, at a rate $\dot{\gamma}$, as calculated, on the one hand, in FE ($\sigma_{xy} = \eta\dot{\gamma}$), and, on the other hand, in MD (where it is obtained through the Irving-Kirkwood formula). The calculations are shown in their full extent in AppendixB and lead to the following formula for a binary mixture of A and B components:

$$\eta = \frac{\pi}{4}\zeta \int_0^\infty \left[n_A^2 g_{AA}(r) + 2n_A n_B g_{AB}(r) + n_B^2 g_{BB}(r)\right] w^2(r)\, r^3 dr,$$

where n_A and n_B are the number densities of A and B constituents in the system, g_{AA}, g_{BB}, and g_{AB} are the radial distribution functions for the $A-A$, $B-B$, and $A-B$ correlations, respectively, and ζ and w are the DPD damping coefficient and the damping function defined in Eq. 2.

For the MD system under consideration, we obtain

$$\eta = 0.726\,\zeta.$$

3.2. Local elastic constants

Having determined the dissipative coefficient of the model, we turn our attention to the *local* elastic properties of the system.

The only relevant material lengthscale in the model being the typical size ($a = 5\sigma_{AA}$) of a rearrangement (Nicolas et al., 2014b), we tile the system into subregions of size a and compute the local stiffness tensors on this "mesoscopic" scale, with the local stress-affine strain method presented in Ref. (Mizuno et al., 2013). Details of this protocol and issues related to the rather unfamiliar local stiffness tensors are discussed in AppendixC. With condensed notations, these tensors can be written as 3×3 real matrices in 2D, *viz.*,

$$\begin{pmatrix} \sigma_{xx} \\ \sigma_{yy} \\ \sqrt{2}\sigma_{xy} \end{pmatrix} = \underbrace{\begin{pmatrix} C_{xx,xx} & C_{xx,yy} & C_{xx,xy} \\ C_{yy,xx} & C_{yy,yy} & C_{yy,xy} \\ C_{xy,xx} & C_{xy,yy} & C_{xy,xy} \end{pmatrix}}_{\mathbf{C}} \begin{pmatrix} \epsilon_{xx} \\ \epsilon_{yy} \\ \sqrt{2}\epsilon_{xy} \end{pmatrix}, \tag{6}$$

where σ_{xx}, σ_{yy}, and σ_{xy} are the linear elastic contributions to the local stress.

Contrary to their macroscopic counterpart, the local $\mathbf{C}$ matrices are not symmetric *a priori*, for very small regions (Tsamados et al., 2009). However, the coarse grain $a = 5\sigma_{AA}$ is large enough here for the assumption of symmetry to be a reasonable approximation. To limit the number of parameters, we further assume that isotropic contraction/dilation of the region only generates an isotropic stress, *i.e.*, that

$$\begin{pmatrix} \epsilon_{xx} & \epsilon_{yy} & \sqrt{2}\epsilon_{xy} \end{pmatrix}^\top = \sqrt{2}/2 \begin{pmatrix} 1 & 1 & 0 \end{pmatrix}^\top$$

is an eigenvector of $\mathbf{C}$.

These two assumptions, namely, tensorial symmetry and isotropy of the response to contraction, imply that the stiffness tensor should be of the form

$$\mathbf{C} = \begin{pmatrix} \alpha & \delta & \beta \\ \delta & \alpha & -\beta \\ \beta & -\beta & \upsilon \end{pmatrix}, \tag{7}$$

where the parameters $\alpha, \delta, \beta, \upsilon \in \mathbb{R}$ are assessed in AppendixC. By analogy with the macroscopic situation, the eigenvalues $c_1 \leqslant c_2 \leqslant c_3$ of the approximated matrix $\mathbf{C}$ are related to the local shear moduli μ_1 and μ_2 and the local bulk modulus K *via* $c_1 = 2\mu_1$, $c_2 = 2\mu_2$, and $c_3 = 2K$, and there exists a frame $(\boldsymbol{e_x}(\theta), \boldsymbol{e_y}(\theta))$, rotated by an angle θ with respect to the original frame, in which the stiffness tensor reads

$$\begin{pmatrix} K+\mu_2 & K-\mu_2 & 0 \\ K-\mu_2 & K+\mu_2 & 0 \\ 0 & 0 & 2\mu_1 \end{pmatrix}, \text{ with } \mu_1 \leqslant \mu_2.$$

Denomination	*Symbol*	*Mean*	*Std dev.*
Shear modulus (weak direction)	μ_1	13.16	7.2
Shear modulus (strong direction)	μ_2	24.46	5.8
Average shear modulus	$\mu \equiv \frac{\mu_1+\mu_2}{2}$	18.81	5.3
Bulk modulus	K	99.9	8.4

Table 1: Statistical properties of the elastic constant distributions: mean values and standard deviations (std dev.).

Consequently, the following four local parameters suffice to determine $\mathbf{C}$ completely: θ, μ_1, μ_2, and K.

Table 1 summarises the main features of the distributions of μ_1, μ_2, and K measured in the Lennard-Jones glass under consideration; θ is uniformly distributed, in accordance with macroscopic isotropy.

It is noteworthy that the local stiffness matrices exhibit significant anisotropy, as indicated by the discrepancy between the mean value of the shear modulus in the (locally) weaker direction, $\langle\mu_1\rangle = 13.16$, and its strong counterpart, $\langle\mu_2\rangle = 24.46$.

Some regions actually even display negative shear moduli μ_1. This is not unrealistic in the MD system, because these regions can be stabilised by the surrounding medium, but in the following they will be discarded, and arbitrarily set to zero, in the FE simulations, where they cause instabilities.

Lastly, the bulk modulus is much larger (by a factor of 5) than the shear moduli, in line with expectations, and its relative standard deviation (*i.e.*, the ratio of the standard deviation and the mean value) is by far smaller than it is for the shear moduli, which means that, on a relative basis, the latter are more broadly distributed. Consequently, we will henceforth always neglect spatial fluctuations of the bulk modulus and set $K = 99.9$. As for the distributions of shear moduli, three types of systems will be considered in FE:

(i) a uniform system, with $\mu_1 = \mu_2 = 18.8$

(ii) a heterogeneous system made of isotropic blocks ("het. iso."), with $\mu_1 = \mu_2 = 18.8 \pm 5.3$, *i.e.*, a normal distribution of shear moduli $\mu_1 = \mu_2$ with mean value 18.8 and standard deviation 5.3. (Remember that each block is a macro-element made of four adjacent finite elements.)

(iii) a heterogeneous system made of anisotropic blocks ("het. aniso."), with $\mu_1 = 13.16 \pm 7.2$ and $\mu_2 = 24.46 \pm 5.8$ and a uniform distribution of the angles θ.

Through the simulation of plane shear waves, we have checked that the transverse sound velocity measured in FE is consistent with that measured in MD.

4. Protocol for the artificially triggered shear transformations

In this section, we describe the protocol to artificially trigger ideal shear transformations.

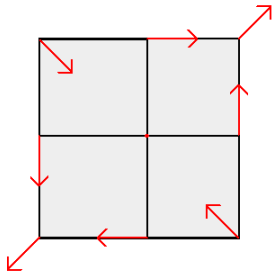

Figure 2: Sketch of the displacements applied to a macro-element to model a pure shear transformation.

In the MD system, following Puosi et al. (2014), shear transformations are artificially created by applying a pure shear strain ϵ_{xy} to a disk centred at (x_0, y_0) and of diameter $a = 5\sigma_{AA}$. To do so, particles whose initial position (x_i, y_i) belongs to this region are moved to a new position (x'_i, y'_i) at $t = 0$, which satisfies

$$\begin{cases} x_i \to x'_i & = x_i + \epsilon_{xy}\,(y_i - y_0) \\ y_i \to y'_i & = y_i + \epsilon_{xy}\,(x_i - x_0)\,. \end{cases}$$

Their positions are then frozen for the whole simulation. In order to measure the elastic, *i.e.*, reversible, response of the medium, ϵ_{xy} never exceeds a few percent strain. Clearly, all (transient or permanent) dilational effects (Schuh et al., 2007) potentially accompanying shear transformations are here discarded.

A similar shear transformation is applied in the FE simulations to a macro-element made of four adjacent elements (see Section 2.2), by controlling the positions of the nodes of these elements, as sketched in Fig. 2.

5. Disorder-averaged propagation of shear waves

Let us first probe the *disorder-averaged* time-dependent response to a shear transformation, in different damping regimes, both in FE and in MD. To this end, MD simulations are averaged over many (50) locations of the shear transformation in the sample, while the FE results are averaged over many (50) realisations of the disorder, *i.e.*, of the random values of the local elastic constants.

5.1. Comparison between MD and Finite Elements

For a quantitative study, we make use of the average propagation radius $\Delta_r(t)$ introduced by Puosi et al. (2014) to measure the advance of the wave,

$$\Delta_r(t) \equiv \iint |u_r(\boldsymbol{r}; t)| d^2\boldsymbol{r},$$

where $u_r(t)$ is the radial displacement at time t. If the final displacement $(u_r(\boldsymbol{r}; t = \infty) \sim r^{-1}$ in any given direction θ in the far field) is essentially achieved as soon as a region is reached by the wavefront, $\Delta_r(t)$ will grow linearly with the (linear) size of the displaced region. The average propagation

radius is plotted in Fig. 5 for diverse values of the damping ζ. The initial growth is ballistic in MD, with $\Delta_r(t) \sim t$, while at long times $\Delta_r(t)$ saturates to its steady-state value. The evolution of $\Delta_r(t)$ before the steady state is reached strongly depends on ζ. At low damping ($\zeta = 1$), the interaction with the waves generated by the periodic replicas of the shear transformation leads to particularly long-lived oscillations of $\Delta_r(t)$ (Fig. 5a), while stronger damping ($\zeta = 100$) completely suppresses these oscillations.

The FE simulations nicely capture this qualitative change, and the agreement both in the limit of low damping (Fig. 5a) and in the limit of strong damping (Fig. 5c) is excellent, at relatively long times. This is true for all three FE systems, including the uniform one, which supports the idea that the *average* propagation in elastically heterogeneous media is virtually identical to the propagation in a uniform medium.

For an intermediate value of the damping, namely, $\zeta = 10$ (Fig. 5b), the agreement is reasonable, but not quite as good, insofar as the oscillations observed in MD are damped perceptibly faster than their counterparts in FE, not only in the uniform system, but also in the heterogeneous one (het. iso.). This suggests that the FE viscosity is somewhat underestimated, or that the anharmonicities present in MD significantly contribute to the damping of the oscillations.

Finally, the short-time propagation is well described at low damping, but the agreement declines when ζ increases, in which case the FE method overestimates the propagation velocity over short distances.

5.2. Theoretical rationalisation

Puosi and co-workers (Puosi et al., 2014) reported that, with a mean-field dissipative force (*i.e.*, by substituting $\boldsymbol{f_i}^D = {}^{-m\boldsymbol{v_i}}/_{\tau_d}$ for Eq. 2 in Eq. 1), $\Delta_r(t)$ initially grows in a diffusive fashion, *i.e.*, $\Delta_r(t) \sim t^{1/2}$, at large damping, that is to say, for short Langevin damping times τ_d. By contrast, no such diffusive regime is observed here, even for large damping parameters ζ. The dissipation scheme therefore affects the nature of shear wave propagation. Can this discrepancy be explained theoretically?

5.2.1. Mean-field dissipation

In the presence of a mean-field damping force, force balance on particle i can schematically be written as

$$m\dot{\boldsymbol{v}}_{\boldsymbol{i}}(t) + \frac{m\boldsymbol{v}_{\boldsymbol{i}}(t)}{\tau_d} \approx k \sum_{\langle j|i \rangle} \left(\boldsymbol{u}_j(t) - \boldsymbol{u}_i(t) \right), \tag{8}$$

where the sum runs over the neighbours j of i, k is a typical stiffness, *i.e.*, the order of magnitude of the relevant Hessian components $\partial^2 V / \partial \boldsymbol{r_i} \partial \boldsymbol{r_j}$, and the $\boldsymbol{u_j}$'s are the displacements with respect to an equilibrium configuration. Let us now introduce a continuous, coarse-grained displacement field $\boldsymbol{u}(\boldsymbol{r}; t)$ and a typical interparticle distance a_0, and substitute the former into Eq. 8, in the overdamped limit $\tau_d \to 0$,

$$\frac{m}{\tau} \frac{\partial \boldsymbol{u}}{\partial t} \approx k a_0^2 \nabla^2 \boldsymbol{u}.$$

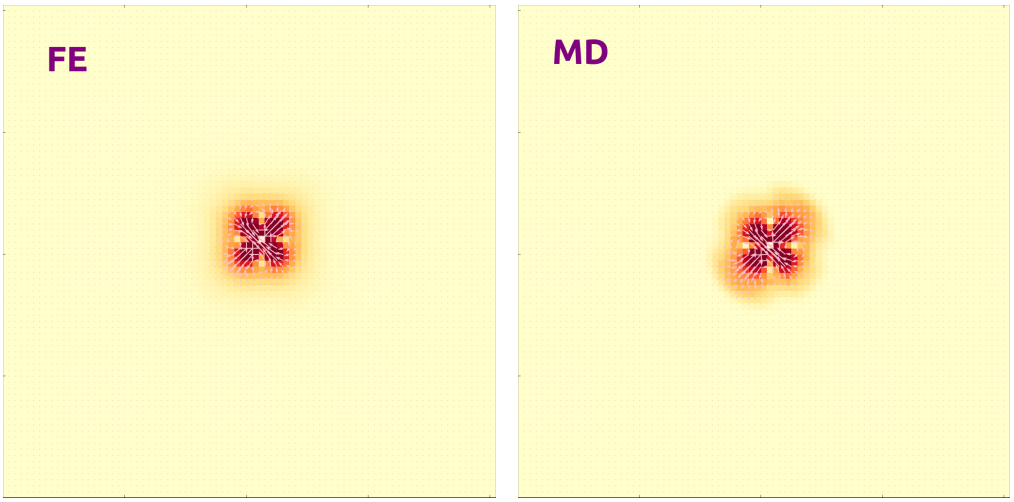

(a) $\Delta t = 2$

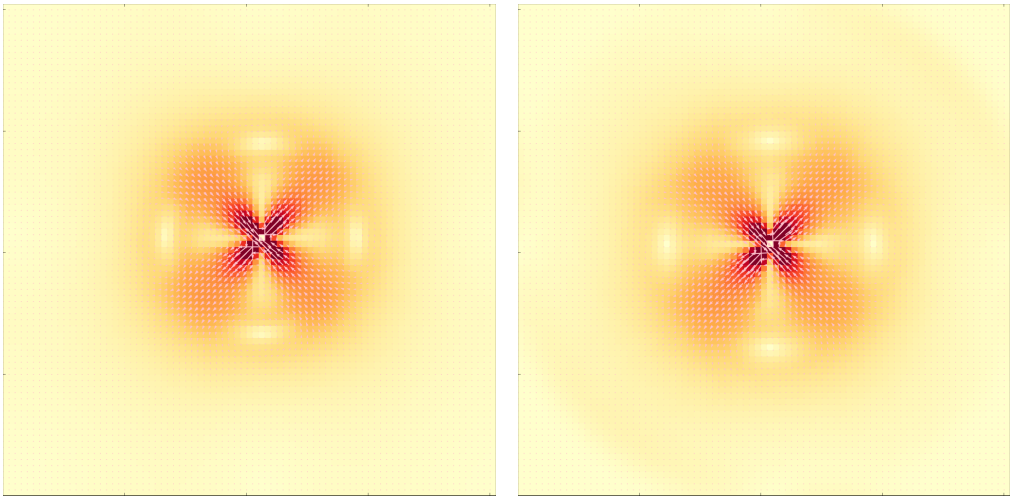

(b) $\Delta t = 10$

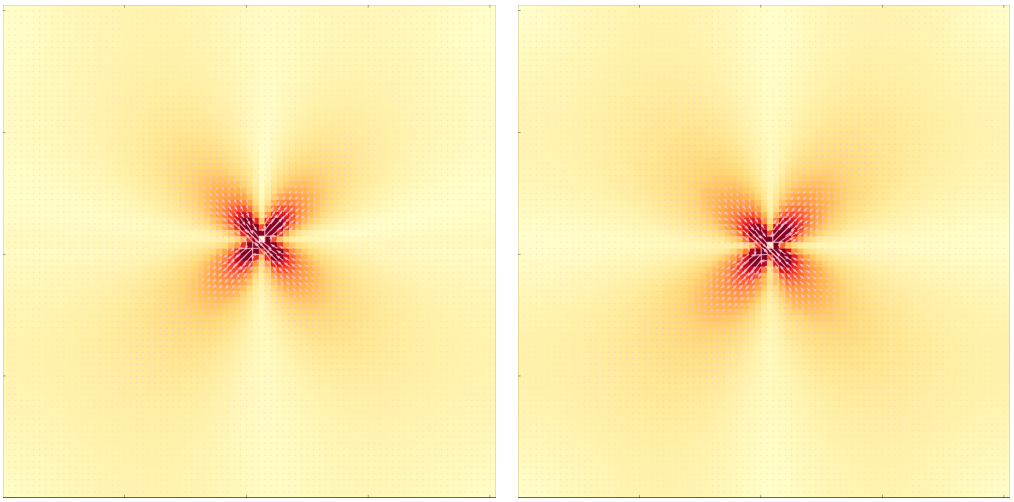

(c) $\Delta t = 1000$

Figure 3: Average displacement field induced by a shear transformation (at the centre of the cell), after a time lag Δt, for $\zeta = 1$. The pink arrows represent the displacement vectors and the background colour indicates their norms. System size: $(205\sigma_{AA})^2$, corresponding to 82^2 finite elements.
(*Left*) Finite Elements, het. iso.; (*right*) Molecular Dynamics.

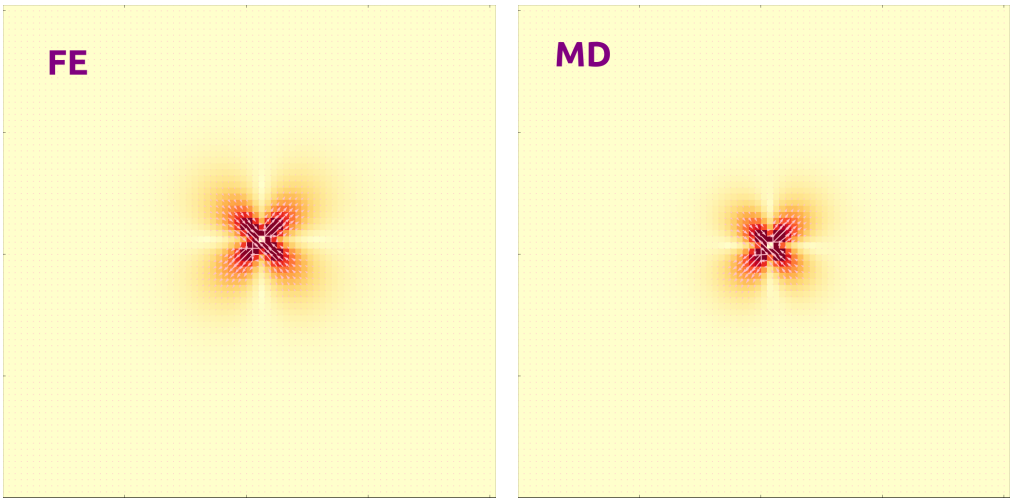

(a) $\Delta t = 2$

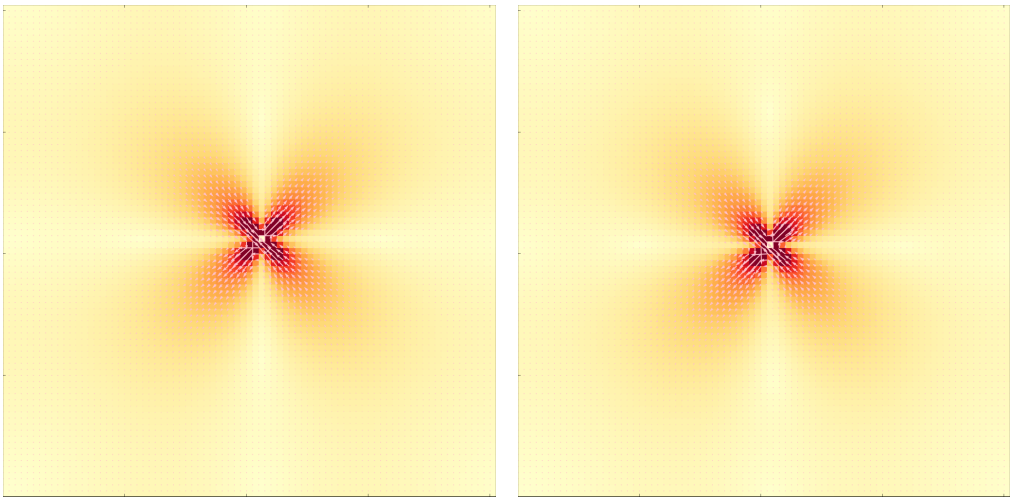

(b) $\Delta t = 10$

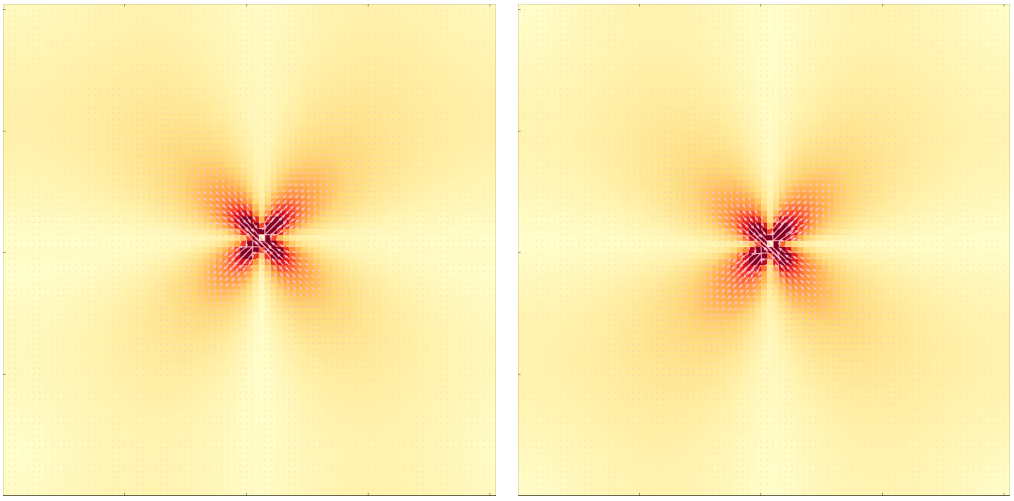

(c) $\Delta t = 1000$

Figure 4: Average displacement field induced by a shear transformation, after a time lag Δt, for strong damping, $\zeta = 100$ (hence, $\eta = 72.6$). Refer to Fig. 3 for the legend.

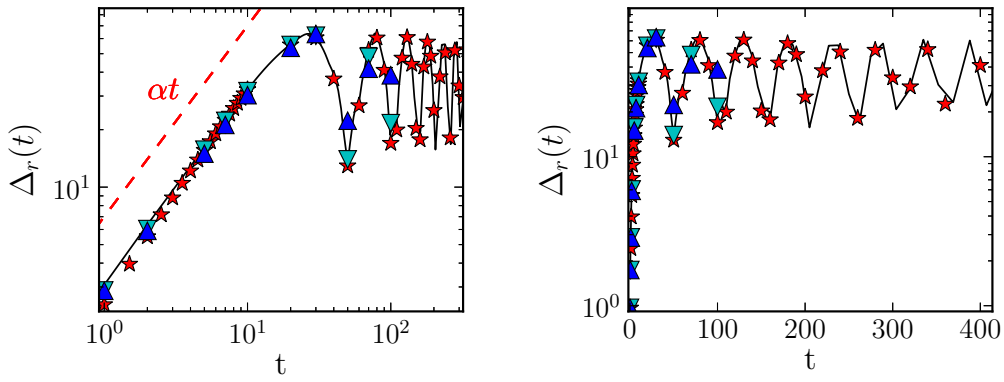

(a) $\zeta = 1$ ($\eta = 0.726$)

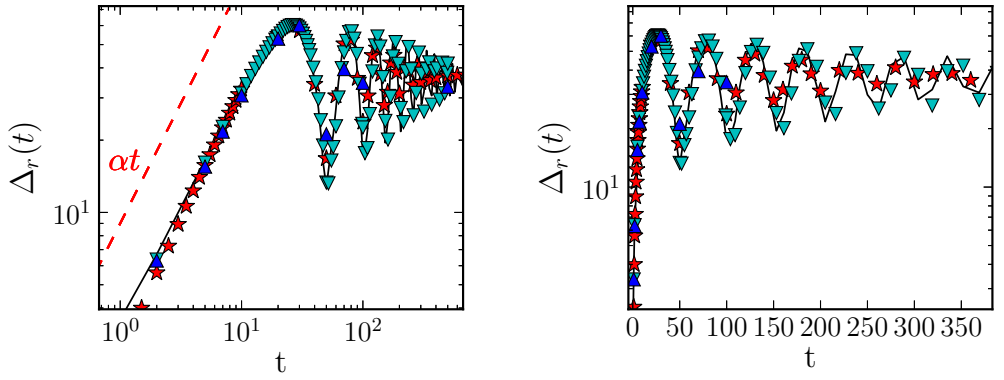

(b) $\zeta = 10$ ($\eta = 7.26$)

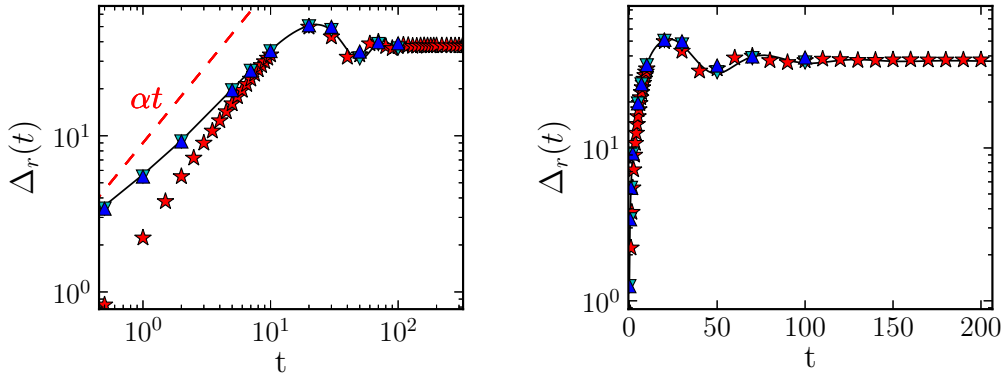

(c) $\zeta = 100$ ($\eta = 72.6$)

Figure 5: Average propagation radius Δ_r as a function of time, for different damping magnitudes.
(*Red stars*) MD data; (*inverted cyan triangles*) FE, het. iso.; (*blue triangles*) FE, het. aniso; (*solid black line*) FE, uniform system.
(*Left*) log-log plot, (*right*) same data, in semi-logarithmic plot.

In this regime of negligible inertia, we thus obtain a diffusive equation for the particle displacements, consistently with the MD observations.

5.2.2. Dissipative Particle Dynamics

Very crudely, the DPD equations of motion (Eqs. 1-2) are approximated by

$$\begin{aligned} m\ddot{\boldsymbol{u}} &\approx \tilde{\zeta}\sum_{\langle j|i\rangle}\left(\dot{\boldsymbol{u}}_j(t)-\dot{\boldsymbol{u}}_i(t)\right)+k\sum_{\langle j|i\rangle}\left(\boldsymbol{u}_j(t)-\boldsymbol{u}_i(t)\right) \\ m\ddot{\boldsymbol{u}} &\approx \tilde{\zeta}a_0^2\nabla^2\dot{\boldsymbol{u}}+ka_0^2\nabla^2\boldsymbol{u}, \end{aligned} \tag{9}$$

where $\tilde{\zeta}\equiv\zeta w^2\left(a_0\right)$.

Equation 9 is a diffusion equation (on $\dot{\boldsymbol{u}}$) *only if* the elastic force is negligible, which will not be the case in practice. (More generally, Eq. 9 can be solved with a space-time Fourier transform, or a joint Laplace-Fourier transform).

It can also be seen in Eq. 9 that, regardless of the value of ζ, the inertial term $m\ddot{\boldsymbol{u}}$ will always dominate at long enough wavelengths. In an unbounded system, this notably implies that the inertialess Brownian limit, which features an infinite transverse sound velocity, is singular.

6. Effect of structural disorder in MD and in FE

Let us now investigate the impact of elastic heterogeneity on the displacement field induced by an individual plastic event, *i.e.*, the importance of fluctuations around the disorder-averaged response.

The norm of the average displacement $\boldsymbol{u}\left(\boldsymbol{r};t\right)$ along a diagonal direction, at a long time lag $\Delta t=1000$, is plotted in Fig. 6 for $\zeta=1$ and $\zeta=100$, along with the associated standard deviation δu, *i.e.,*

$$\delta u\left(\boldsymbol{r};t\right)=\sqrt{\left\langle\left[\boldsymbol{u}^{(d)}\left(\boldsymbol{r};t\right)-\boldsymbol{u}\left(\boldsymbol{r};t\right)\right]^2\right\rangle_d},$$

where the brackets denote an average over the realisations of disorder. Incidentally, one may notice that, for $\zeta=1$ (Fig. 6a), MD and FE do not coincide satisfactorily with respect to the average displacements, but this is mostly due to a loss of synchronization: the oscillations described in Section 5.1 have not died out yet at this time lag and they are not exactly in phase in the different systems. Had the true steady-state limit, $\Delta t\to\infty$, been reached (at the expense of much longer simulations), we would have expected much better agreement on the average displacements. This expectation is supported by the coincidence of the average displacements at $\Delta t=1000$ under strong damping, for $\zeta=100$ (see Fig. 6b), in which case dissipation is more efficient and the steady state is reached after fewer MD steps; indeed, in the linear regime probed here, the final state should be independent of the dynamics, hence of ζ.

Regarding the fluctuations, the main result is that their order of magnitude is well reproduced by the FE simulations, both with isotropic blocks (het. iso., $\mu_1=\mu_2$) and with anisotropic blocks (het. aniso.), although, quite naturally, het. aniso. displays larger fluctuations than het. iso. Moreover, it

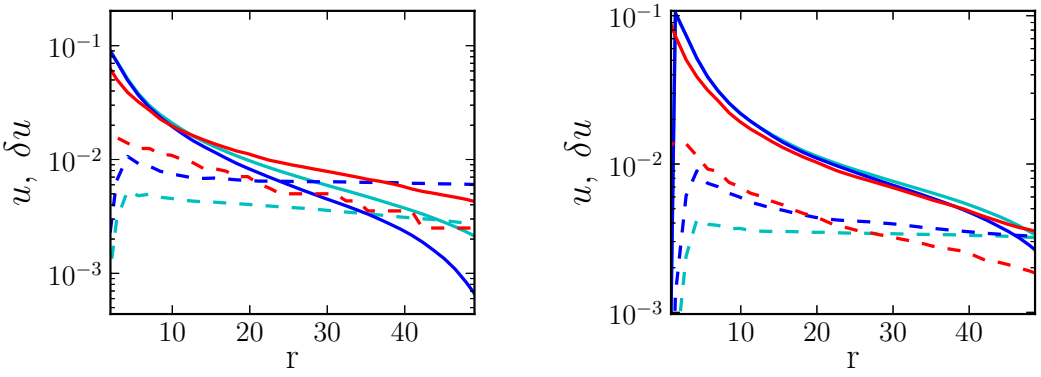

(a) $\zeta = 1$. (b) $\zeta = 100$.

Figure 6: (*Solid lines*) mean value u and (*dashed lines*) standard deviation δu of the displacement norm along a diagonal axis $\boldsymbol{e}_{\text{diag}} = \frac{\sqrt{2}}{2}(\boldsymbol{e}_{\boldsymbol{x}} + \boldsymbol{e}_{\boldsymbol{y}})$, after a time lag $\Delta t = 1000$, as a function of the distance (in FE units). (*Red*) MD; (*cyan*) FE, het. iso.; (*blue*) FE, het. aniso.

is noteworthy that these corrections δu are roughly half as large as the mean reponse at a distance of, *e.g.*, $50\sigma_{AA}$. To avoid any misunderstanding on the possible nature of the fluctuations measured in MD, let us recall here that the centre of mass of the MD simulation cell is kept fixed, which prevents the variable global translations of the system that are sometimes observed otherwise (and which then dominate the fluctuations)[3].

With regard to the spatial distribution of δu, colour maps of the relative fluctuations $\delta u(\boldsymbol{r};t)/u(\boldsymbol{r};t)$ are presented in Fig. 7. In regions with non-negligible displacements, *i.e.*, $u(\boldsymbol{r};t) \geqslant 10^{-2}$, the relative fluctuations are approximately homogeneous and tend to increase slightly with time.

In conclusion to this section, taking into account the broad distribution of shear moduli in FE has enabled us to recover the fluctuations observed in MD. This further confirms the role of structural disorder on the redistribution of stress induced by a plastic event. In the last section, we go one step further by attempting to reproduce the individual, time-dependent response to a *given* plastic event in MD with the simple FE framework.

7. Time-dependent response to a particular plastic event

Even though the study of the propagation dynamics (Section 5) and of disorder-induced fluctuations (Section 6) validates the FE method for (future) use in, *e.g.*, mesoscopic rheological models, we would like to know whether the comparison can be pushed further. More precisely, can the FE routine describe the details of the elastic response in a *particular* configuration?

3. When the centre of mass of the MD simulation cell is not kept fixed, the fluctuations δu measured in MD are significantly larger and their profile with respect to the distance r to the origin (dashed lines in Fig. 6) is almost flat.

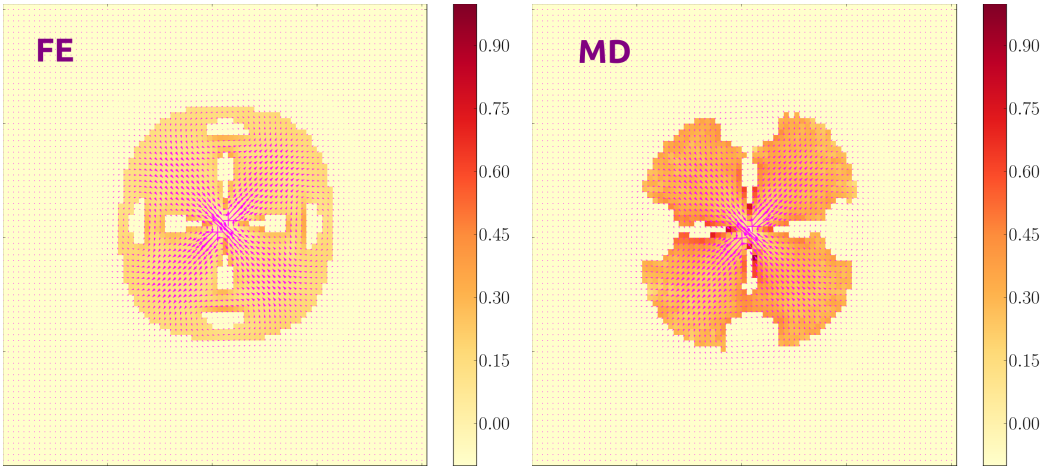

(a) $\Delta t = 10$

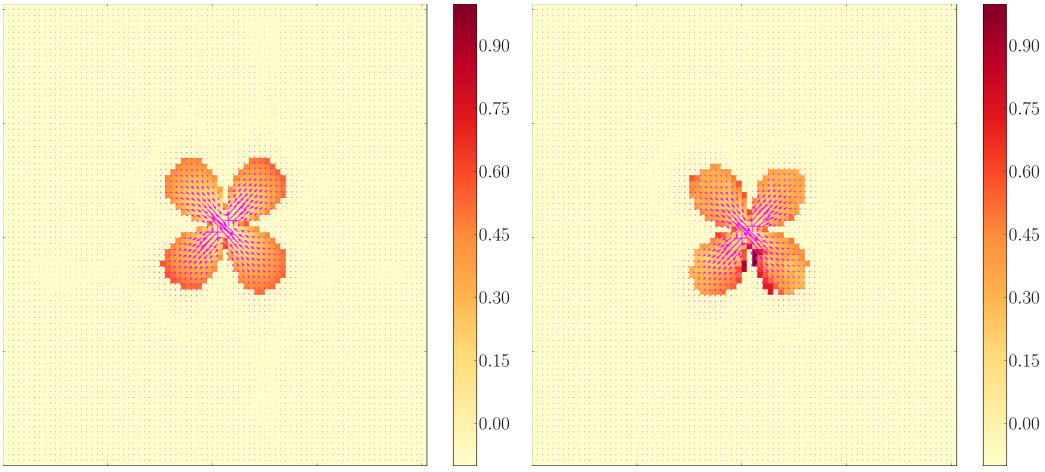

(b) $\Delta t = 100$

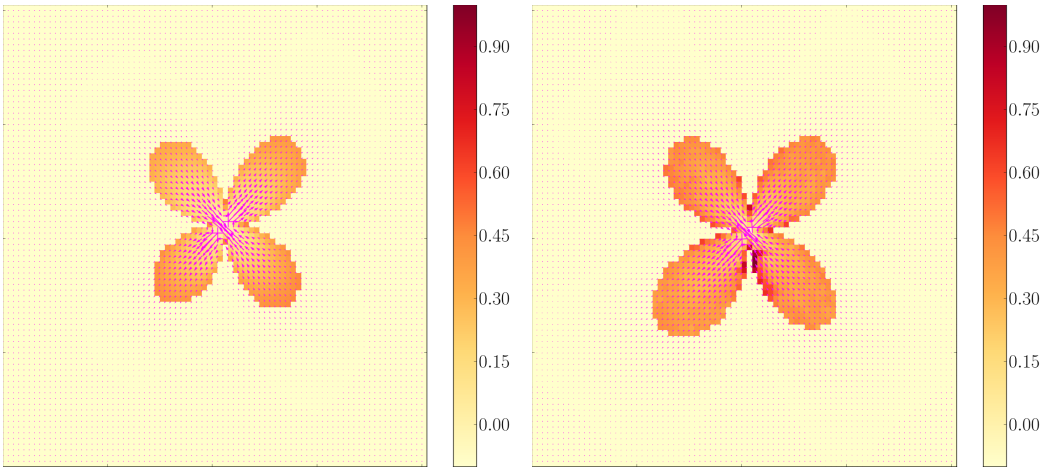

(c) $\Delta t = 1000$

Figure 7: Colour map of the relative displacement norm fluctuations $\delta u(\boldsymbol{r};t)/u(\boldsymbol{r};t)$ for $\zeta = 1$. The regions where $u(\boldsymbol{r};t) < 10^{-2}$ are overlaid in light yellow.

To address this question, within the third type of FE mode, namely, het. aniso., the local shear moduli μ_1 and μ_2 and the angle θ of each FE macro-element (*i.e.,* set of four adjacent elements) are directly extracted from the corresponding region in the MD system. Then, we compute the coarse-grained strain field [4] induced by shear transformations occurring at given position in the sample, an example of which is shown in Fig. 8.

Clearly, the MD response and its FE counterpart look alike and both exhibit the distinctive quadrupolar angular structure associated to the response in a uniform medium. However, are the disorder-induced fluctuations, *i.e*, the deviations from this average response, also similar in MD and FE? In an endeavour to answer this question, we have looked at the *deviations* in half a dozen particular configurations (*not shown*) and considered a couple of basic measures of similarity, but our results remain inconclusive in this respect: there is no quantifiable evidence that the disorder-induced fluctuations in a particular MD configuration are satisfactorily reproduced in FE.

8. Conclusions

In conclusion, we have extracted information about the local elastic constants of a binary Lennard-Jones mixture and the viscosity associated with a DPD damping scheme. Consistently with the findings of Mizuno et al. (2013), we have found that the local shear moduli are more broadly distributed (on a relative basis) than local bulk moduli.

These elastic and viscous properties were used as input in a simple FE routine and an ideal shear transformation was artificially triggered in the (FE and MD) systems.

We observed that the *average* time-dependent elastic response to this transformation in a disordered medium is similar to the propagation in a uniform medium and it is well reproduced in the FE simulations. However, fluctuations with respect to the average displacement field are considerable, with relative fluctuations of a few tens of percents. The approximate magnitude of these fluctuations is captured by FE simulations on heterogeneous, but locally isotropic systems. Refining the description by considering the elastic anisotropy on the mesoscale does not play a major role in this respect.

It should however be stressed that, throughout our investigation, shear transformations were arbitrarily imposed, through an instantaneous displacement of particles (or FE nodes). However, in a *bona fide* simulation, the dynamics of shear transformations are determined by the system itself; two dynamical regimes can then be envisioned:

(i) if inertia is negligible, the competitition between elasticity and viscosity sets the timescale of the rearrangement, $\tau = \eta/\mu$,

(ii) if the rearrangement mostly consists in the damping of the inertial force (initially generated by elasticity), then the duration of a rearrangement is set by the inverse damping coefficient ζ^{-1}.

4. In MD, local strains are computed after coarse-graining the displacement field on a grid similar to the FE one; note that the strain field is expected to be less sensitive to heterogeneities than the displacement field.

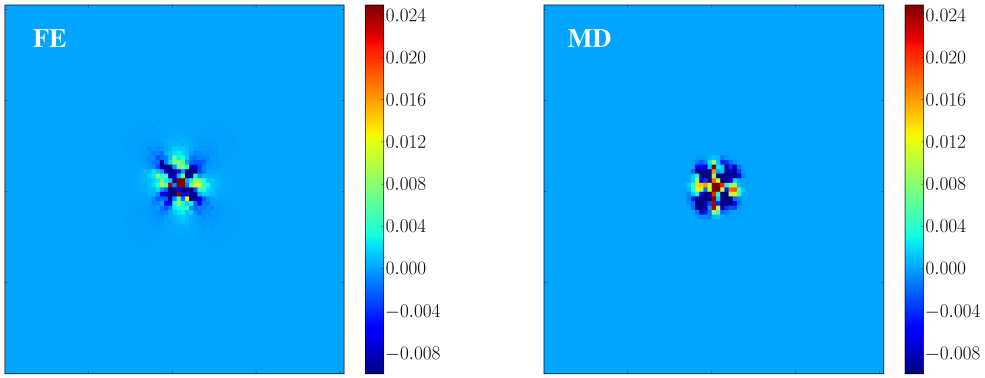

(a) $\Delta t = 1$

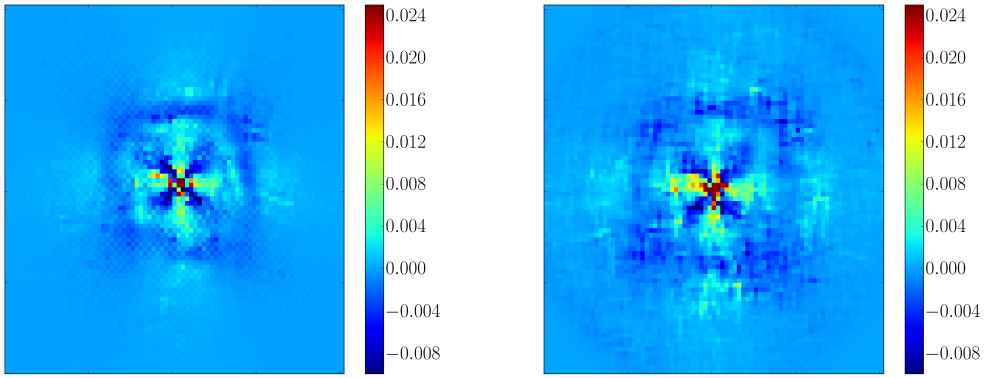

(b) $\Delta t = 10$

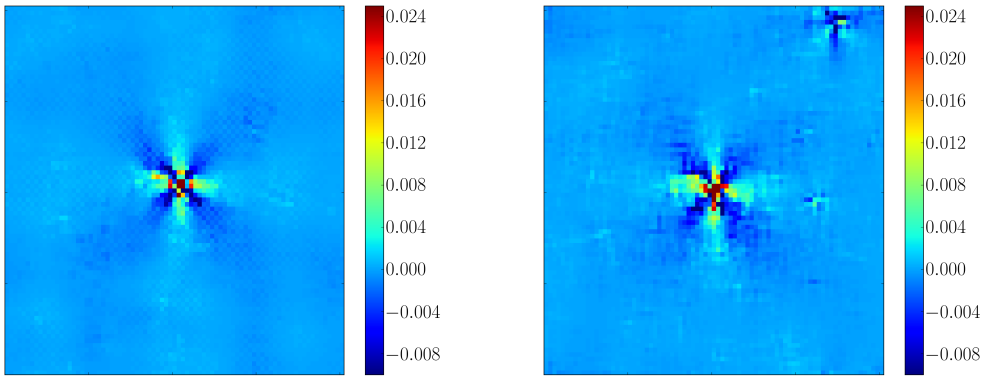

(c) $\Delta t = 100$

Figure 8: Local strain field induced by a particular shear transformation at different lag times, for $\zeta = 1$.
(*Left*) FE, with an elastic configuration modelled on the MD system; (*right*) MD.

All in all, our method represents a powerful new framework for rheological models for amorphous solids, which improves on the traditional use of an analytical elastic propagator and the computation of the response by means of a Fast Fourier Transform, in that it accounts for structural disorder and inertial effects, whose impact has been underscored by Salerno et al. (2012), it can be extended to arbitrary (in particular, confined) geometries, and it may include pre-existing local defects in the material, such as cracks. A further asset of this strategy is that, notwithstanding the enhanced capabilities of the algorithm, its complexity in terms of number of operations scales linearly with the number of blocks (or FE cells) for large systems, that is, with a scaling comparable to that of the Fast Fourier Transform routine.

Acknowledgements

AN thanks Richard MICHEL for his help with the Finite Element method. The MD simulations were carried out on clusters belonging to the CIMENT infrastructure (https://ciment.ujf-grenoble.fr), which is supported by the Rhône-Alpes region (GRANT CPER07_13 CIRA: http://www.ci-ra.org), using LAMMPS molecular dynamics software Plimpton (1995) (http: //lammps.sandia.gov). JLB is supported by Institut Universitaire de France and by grant ERC-2011-ADG20110209.

Bibliography

Amon, A., Bruand, A., Crassous, J., Clément, E., et al., 2012. Hot spots in an athermal system. Physical Review Letters 108 (13), 135502.

Argon, A., Kuo, H., 1979. Plastic flow in a disordered bubble raft (an analog of a metallic glass). Materials Science and Engineering 39 (1), 101–109.

Berthier, L., Biroli, G., 2011. Theoretical perspective on the glass transition and amorphous materials. Reviews of Modern Physics 83 (2), 587.

Budrikis, Z., Zapperi, S., 2013. Avalanche localization and crossover scaling in amorphous plasticity. Physical Review E 88 (6), 062403.

Chandler, D., Garrahan, J., 2010. Dynamics on the way to forming glass: Bubbles in space-time. Annual Review of Physical Chemistry 61 (1), 191–217.

Desmond, K. W., Weeks, E. R., 2013. Experimental measurements of stress redistribution in flowing emulsions. arXiv preprint arXiv:1306.0269.

Eshelby, J., 1957. The Determination of the Elastic Field of an Ellipsoidal Inclusion, and Related Problems. Proceedings of the Royal Society A: Mathematical, Physical and Engineering Sciences 241 (1226), 376–396.

Falk, M., Langer, J., 1998. Dynamics of viscoplastic deformation in amorphous solids. Physical Review E 57 (6), 7192–7205.

Lin, J., Saade, A., Lerner, E., Rosso, A., Wyart, M., 2014. On the density of shear transformations in amorphous solids. Europhysics Letters (EPL) 105 (2), 26003–26009.

Lubchenko, V., Wolynes, P., 2007. Theory of structural glasses and supercooled liquids. Annu. Rev. Phys. Chem. 58, 235–266.

Martens, K., Bocquet, L., Barrat, J.-L., 2011. Connecting diffusion and dynamical heterogeneities in actively deformed amorphous systems. Physical Review Letters 106 (15), 156001.

Martens, K., Bocquet, L., Barrat, J.-L., 2012. Spontaneous formation of permanent shear bands in a mesoscopic model of flowing disordered matter. Soft Matter 8 (15), 4197–4205.

Mizuno, H., Mossa, S., Barrat, J.-L., 2013. Measuring spatial distribution of the local elastic modulus in glasses. Physical Review E 87 (4), 042306.

Nicolas, A., Martens, K., Bocquet, L., Barrat, J.-L., 2014a. Universal and non-universal features in coarse-grained models of flow in disordered solids. Soft Matter 10, 4648–4661.

Nicolas, A., Rottler, J., Barrat, J.-L., 2014b. Spatiotemporal correlations between plastic events in the shear flow of athermal amorphous solids. The European Physical Journal E 37 (6).

Picard, G., Ajdari, A., Lequeux, F., Bocquet, L., 2004. Elastic consequences of a single plastic event: a step towards the microscopic modeling of the flow of yield stress fluids. The European physical journal. E, Soft matter 15 (4), 371–81.

Picard, G., Ajdari, A., Lequeux, F., Bocquet, L., 2005. Slow flows of yield stress fluids: Complex spatiotemporal behavior within a simple elastoplastic model. Physical Review E 71 (1), 010501.

Plimpton, S., 1995. Fast parallel algorithms for short-range molecular dynamics. Journal of computational physics 117 (1), 1–19.

Puosi, F., Rottler, J., Barrat, J.-L., 2014. Time-dependent elastic response to a local shear transformation in amorphous solids. Physical Review E 89, 042302.

Rottler, J., Schoenholz, S., Liu, A., 2014. Predicting plasticity with soft vibrational modes: From dislocations to glasses. Physical Review E 89 (4), 042304.

Salerno, K., Maloney, C. E., Robbins, M. O., 2012. Avalanches in Strained Amorphous Solids: Does Inertia Destroy Critical Behavior? Physical Review Letters 109 (10), 105703.

Salerno, K. M., Robbins, M. O., 2013. Effect of inertia on sheared disordered solids: Critical scaling of avalanches in two and three dimensions. Physical Review E 88 (6), 062206.

Sandfeld, S., Budrikis, Z., Zapperi, S., Castellanos, D. F., 2015. Avalanches, loading and finite size effects in 2d amorphous plasticity: results from a finite element model. Journal of Statistical Mechanics: Theory and Experiment 2015 (2), P02011.
URL http://stacks.iop.org/1742-5468/2015/i=2/a=P02011

Schall, P., Weitz, D., Spaepen, F., 2007. Structural rearrangements that govern flow in colloidal glasses. Science (New York, N.Y.) 318 (5858), 1895–9.

Schuh, C., Hufnagel, T., Ramamurty, U., 2007. Mechanical behavior of amorphous alloys. Acta Materialia 55 (12), 4067–4109.

Soddemann, T., Dünweg, B., Kremer, K., 2003. Dissipative particle dynamics: A useful thermostat for equilibrium and nonequilibrium molecular dynamics simulations. Physical Review E 68 (4), 046702.

Talamali, M., Petäjä, V., Vandembroucq, D., Roux, S., 2011. Avalanches, precursors, and finite-size fluctuations in a mesoscopic model of amorphous plasticity. Physical Review E 84 (1).

Tsamados, M., Tanguy, A., Goldenberg, C., Barrat, J.-L., 2009. Local elasticity map and plasticity in a model Lennard-Jones glass. Physical Review E 80 (2).

Vandembroucq, D., Roux, S., 2011. Mechanical noise dependent aging and shear banding behavior of a mesoscopic model of amorphous plasticity. Physical Review B 84 (13), 134210.

Varnik, F., Mandal, S., Chikkadi, V., Denisov, D., Olsson, P., Vågberg, D., Raabe, D., Schall, P., 2014. Correlations of plasticity in sheared glasses. arXiv preprint arXiv:1401.3986.

Widmer-Cooper, A., Perry, H., Harrowell, P., Reichman, D., 2008. Irreversible reorganization in a supercooled liquid originates from localized soft modes. Nature Physics 4 (9), 711–715.

AppendixA. Simplified Finite Element routine

Bearing in mind our pursuit of minimalism, we choose a simple regular square meshgrid, as sketched in Fig. 1. If one assumes that the strain and stress fields are approximately uniform in each element, the following equations can be written between the (nodal) displacements (u_x, u_y) and the (elemental) strains $\boldsymbol{\epsilon}$, on the one hand, and the (nodal) forces $\left(f_x^{\mathrm{el}}, f_y^{\mathrm{el}}\right)$ and the (elemental) stresses $\boldsymbol{\sigma}$, on the other hand:

$$\boldsymbol{\epsilon} = \mathbf{B} \cdot \begin{pmatrix} u_x^{(0)} \\ u_y^{(0)} \\ \vdots \\ u_x^{(3)} \\ u_y^{(3)} \end{pmatrix} \text{ and } \boldsymbol{\sigma} = -\mathbf{B} \cdot \begin{pmatrix} f_x^{\mathrm{el}\,(0)} \\ f_y^{\mathrm{el}\,(0)} \\ \vdots \\ f_x^{\mathrm{el}\,(3)} \\ f_y^{\mathrm{el}\,(3)} \end{pmatrix}, \tag{A.1}$$

where the nodes of the element have been numbered from 0 to 3 counter-clockwise, starting from the bottom left corner, *viz.*, $\begin{smallmatrix}3\\0\end{smallmatrix}\square\begin{smallmatrix}2\\1\end{smallmatrix}$, and $u_x^{(0)}$ denotes the displacement along x at the (0) node, *etc.* Here, we have used condensed notations for the 2D strains and the stresses, *viz.*,

$$\boldsymbol{\epsilon} \equiv \begin{pmatrix} \epsilon_{xx} \\ \epsilon_{yy} \\ \sqrt{2}\epsilon_{xy} \end{pmatrix} \text{ and } \boldsymbol{\sigma} \equiv \begin{pmatrix} \sigma_{xx}^{\mathrm{el}} \\ \sigma_{yy}^{\mathrm{el}} \\ \sqrt{2}\sigma_{xy}^{\mathrm{el}} \end{pmatrix},$$

and the matrix $\mathbf{B}$ is given by

$$\mathbf{B} \equiv {}^1\!/_2 \begin{bmatrix} -1 & & 1 & & 1 & & -1 & \\ & -1 & & -1 & & 1 & & 1 \\ {}^{-1}\!/_{\sqrt{2}} & {}^{-1}\!/_{\sqrt{2}} & {}^{-1}\!/_{\sqrt{2}} & {}^{1}\!/_{\sqrt{2}} & {}^{1}\!/_{\sqrt{2}} & {}^{1}\!/_{\sqrt{2}} & {}^{1}\!/_{\sqrt{2}} & {}^{-1}\!/_{\sqrt{2}} \end{bmatrix}.$$

Notice that our simplified FE method is close to a Finite Volume method, in practice. The $\sqrt{2}$ prefactors have been introduced with foresight (see Section 3.2) and the "minus" sign preceding $\mathbf{B}$ in Eq. A.1 should not come as a surprise if one recalls that $\boldsymbol{f}^{\mathrm{el}\,(i)}$ is the force exerted *by* the element *on* node i.

Contrary to traditional FE codes, the mesh will here remain static, *i.e.*, not be distorted owing to the material deformation.

AnnexeA.1. Elastic force-displacement matrix

The objective is now to rewrite Eq. 3 in terms of nodal displacements and forces in order to arrive at Eq. 4.

To relate the nodal displacements and the nodal forces in each element, we make use of the constitutive equation of the material.

To start with, the elastic contribution is governed by Hooke's law, which reads, in condensed notations (Tsamados et al., 2009),

$$\boldsymbol{\sigma} = \mathbf{C} \cdot \boldsymbol{\epsilon}, \tag{A.2}$$

where $\mathbf{C}$ is a 3×3 real matrix. Substituting from Eq. A.1, one obtains the local relation between the forces exerted on the nodes by the material element under consideration and the displacements at the nodes, *viz.*,

$$\begin{pmatrix} f_x^{\mathrm{el}\,(0)} \\ f_y^{\mathrm{el}\,(0)} \\ \vdots \\ f_x^{\mathrm{el}\,(3)} \\ f_y^{\mathrm{el}\,(3)} \end{pmatrix} = -\mathbf{B}^\top \mathbf{C} \mathbf{B} \cdot \begin{pmatrix} u_x^{(0)} \\ u_y^{(0)} \\ \vdots \\ u_x^{(3)} \\ u_y^{(3)} \end{pmatrix}. \tag{A.3}$$

To proceed, the *local* elastic force-displacement matrices $\mathbf{K} \equiv -\mathbf{B}^\top \mathbf{C} \mathbf{B}$ are assembled into a global elastic force-displacement matrix $\boldsymbol{\mathcal{K}}$, *viz.*,

$$\begin{pmatrix} f_x^{\mathrm{el}\,(\mathbf{N-1})} \\ f_y^{\mathrm{el}\,(\mathbf{N-1})} \\ \vdots \\ f_x^{\mathrm{el}\,(\mathbf{0})} \\ f_y^{\mathrm{el}\,(\mathbf{0})} \end{pmatrix} = \boldsymbol{\mathcal{K}} \cdot \begin{pmatrix} u_x^{(\mathbf{N-1})} \\ u_y^{(\mathbf{N-1})} \\ \vdots \\ u_x^{(\mathbf{0})} \\ u_y^{(\mathbf{0})} \end{pmatrix},$$

where the bold superscripts refer to the global labels used in Fig. 1, by opposition with the elemental labels used in Eq. A.3. Here, $\boldsymbol{\mathcal{K}}$ is a sparse $2N \times 2N$ matrix.

AppendixA.2. Viscous force-velocity matrix

The foregoing derivation relies on the linear relation connecting local strains and elastic stresses. Thus, it can straightforwardly be extended to the viscous stresses, insofar as they are linearly related with the local strain rates, *viz.*,

$$\dot{\boldsymbol{\sigma}}^{\mathrm{diss}} = \mathbf{C}^{\mathbf{diss}} \cdot \dot{\boldsymbol{\epsilon}}. \tag{A.4}$$

Globally, the viscous force-velocity relation reads

$$\begin{pmatrix} f_x^{\mathrm{diss}\,(\mathbf{N-1})} \\ f_y^{\mathrm{diss}\,(\mathbf{N-1})} \\ \vdots \\ f_x^{\mathrm{diss}\,(\mathbf{0})} \\ f_y^{\mathrm{diss}\,(\mathbf{0})} \end{pmatrix} = \boldsymbol{\mathcal{H}} \cdot \begin{pmatrix} \dot{u}_x^{(\mathbf{N-1})} \\ \dot{u}_y^{(\mathbf{N-1})} \\ \vdots \\ \dot{u}_x^{(\mathbf{0})} \\ \dot{u}_y^{(\mathbf{0})} \end{pmatrix},$$

where the $2N \times 2N$ matrix $\boldsymbol{\mathcal{H}}$ has been assembled from elemental matrices of the form $-\mathbf{B}^\top \mathbf{C}^{\mathbf{diss}} \mathbf{B}$.

AppendixA.3. Inertial force-acceleration matrix

Finally, we must express the inertial forces, that is to say, the matrix $\boldsymbol{\mathcal{M}}$ in Eq. 4. The convected part of the material derivative of the velocity, namely, $\boldsymbol{v} \cdot (\nabla \boldsymbol{v})$, which scales with v^2 for elements of unit size, is neglected.

We compute the inertial forces directly at the nodes. In other words, each node is assigned a mass $m_0 \equiv \rho V_0$, where V_0 is the elemental volume (*i.e.*, area). Accordingly, the lumped-mass matrix $\boldsymbol{\mathcal{M}}$ connecting the accelerations at the nodes to the inertial forces at the nodes is a $2N \times 2N$ matrix with m_0 on the diagonal, *i.e.*,

$$\boldsymbol{\mathcal{M}} = \begin{pmatrix} m_0 & & \\ & \ddots & \\ & & m_0 \end{pmatrix}.$$

Below, we detail the steps and approximations that bridge the gap between the Continuum Mechanics formulation of Eq. 3 and the following FE problem,

$$\underbrace{\boldsymbol{\mathcal{M}} \begin{pmatrix} \ddot{u}_x^{(\mathbf{N-1})} \\ \ddot{u}_y^{(\mathbf{N-1})} \\ \vdots \\ \ddot{u}_x^{(\mathbf{0})} \\ \ddot{u}_y^{(\mathbf{0})} \end{pmatrix}}_{\text{inertial force}} = \underbrace{\boldsymbol{\mathcal{K}} \begin{pmatrix} u_x^{(\mathbf{N-1})} \\ u_y^{(\mathbf{N-1})} \\ \vdots \\ u_x^{(\mathbf{0})} \\ u_y^{(\mathbf{0})} \end{pmatrix}}_{\text{elasticity}} + \underbrace{\boldsymbol{\mathcal{H}} \begin{pmatrix} \dot{u}_x^{(\mathbf{N-1})} \\ \dot{u}_y^{(\mathbf{N-1})} \\ \vdots \\ \dot{u}_x^{(\mathbf{0})} \\ \dot{u}_y^{(\mathbf{0})} \end{pmatrix}}_{\text{viscosity}}, \tag{A.5}$$

where the $u_x^{(\mathbf{i})}$'s and $u_y^{(\mathbf{i})}$'s are the displacements at the nodes $i \in \{0, \ldots, N-1\}$ of a regular mesh.

AppendixA.4. Discretisation of the dynamics

A central difference scheme is used to discretise Eq. A.5 in time, *viz.*,

$$\begin{aligned} \delta\dot{u}\left(t_n\right) &= \frac{\delta u\left(t_{n+1}\right)-\delta u\left(t_{n-1}\right)}{2\delta t}+\mathcal{O}(\delta t^2) \\ \delta\ddot{u}\left(t_n\right) &= \frac{\delta u\left(t_{n+1}\right)+\delta u\left(t_{n-1}\right)-2\delta u\left(t_n\right)}{\delta t^2}+\mathcal{O}(\delta t), \end{aligned} \tag{A.6}$$

where t_{n-1}, t_n, and t_{n+1} refer to consecutive time , separated by a fixed time step δt.

After insertion into Eq. A.5, provided that $\delta u(t_{n-1})$ and $\delta u(t_n)$ are known, the displacements at the next time step $\delta u(t_{n+1})$ are straightforwardly obtained by inverting a matrix. The advantage of using a static meshgrid is that this matrix is then constant and, accordingly, can be inverted once and for all at the beginning of the simulation.

AppendixA.5. Biperiodic boundary conditions

We implement biperiodic boundary conditions by connecting the leftmost nodes of the system to the rightmost ones (see Fig. 1), and the top row to the bottom one.

AppendixB. Relation between the intrinsic macroscopic viscosity and the microscopic damping coefficient

In MD, the damping magnitude is set by the coefficient ζ in the expression of the dissipative force $\boldsymbol{f_i}^D$ (Eq. 2), whereas it is set by the viscosity η in FE. In order to match the damping in both simulations, we must connect the MD dissipative force $\boldsymbol{f_i}^D$ to the viscous stress in FE, namely, $\boldsymbol{\sigma}^{\mathbf{diss}} = 2\eta\dot{\boldsymbol{\epsilon}}$ (see Eq. 3).

To this end, we consider a pure shear situation, in which particles are strictly advected by the flow

$$\begin{aligned} \boldsymbol{v}(\boldsymbol{r}) &= \dot{\boldsymbol{\epsilon}}\cdot\boldsymbol{r} \\ \text{with } \dot{\boldsymbol{\epsilon}} &\equiv \dot{\epsilon}_{xy}\left(\boldsymbol{e_y}\otimes\boldsymbol{e_x}+\boldsymbol{e_x}\otimes\boldsymbol{e_y}\right). \end{aligned}$$

On the one hand, in MD, the microscopic dissipative stress on particle i (of volume V_0) is obtained with the help of the Irving-Kirkwood formula, *viz.*,

$$\begin{aligned} \boldsymbol{\sigma}(\boldsymbol{r_i}) &= V_0^{-1}\sum_j \boldsymbol{r_{ij}}\otimes\boldsymbol{f_{ij}^D} \\ &= -\zeta V_0^{-1}\sum_j w^2\left(r_{ij}\right)\frac{\boldsymbol{v_{ij}}\cdot\boldsymbol{r_{ij}}}{r_{ij}^2}\boldsymbol{r_{ij}}\otimes\boldsymbol{r_{ij}}. \end{aligned}$$

Focusing on the xy-component of the stress and setting $\boldsymbol{r_i}$ as the origin of the

frame, *i.e.*, $\boldsymbol{r_i} = \mathbf{0}$, for convenience, we get

$$\begin{aligned}
\sigma_{xy}(\boldsymbol{r_i} = \mathbf{0}) &= \zeta V_0^{-1} \sum_j w^2(r_j) \frac{\boldsymbol{v_j} \cdot \boldsymbol{r_j}}{r_j^2} x_j y_j \\
&= \zeta \dot{\epsilon}_{xy} V_0^{-1} \sum_j w^2(r_j) \frac{2 y_j x_j}{r_j^2} x_j y_j \\
&\simeq 2\zeta \dot{\epsilon}_{xy} V_0^{-1} \iint n g(r) w^2(r) \frac{x^2 y^2}{r^2} d^2 r \\
&= 2\zeta n \dot{\epsilon}_{xy} V_0^{-1} \int_0^{2\pi} \cos^2(\theta) \sin^2(\theta) d\theta \int_0^{\infty} g(r) w^2(r) r^3 dr \qquad \text{(B.1)} \\
&= \frac{\pi}{2} \zeta n \dot{\epsilon}_{xy} V_0^{-1} \int_0^{\infty} g(r) w^2(r) r^3 dr.
\end{aligned}$$

Here, n is the average number density of the system and $g(r)$ is the (alledgedly isotropic) pair correlation function. Equation B.1 expresses the stress in a volume of space occupied by a particle; elsewhere the stress is zero. Therefore, the average stress in the material reads

$$\begin{aligned}
\overline{\sigma_{xy}} &= (n V_0) \sigma_{xy}(\boldsymbol{r_i} = \mathbf{0}) \\
&= \frac{\pi}{2} \zeta \dot{\epsilon}_{xy} n^2 \int_0^{\infty} g(r) w^2(r) r^3 dr
\end{aligned}$$

On the other hand, in FE, the shear stress simply obeys $\overline{\sigma_{xy}} = 2\eta \dot{\epsilon}_{xy}$. It immediately follows that

$$\boxed{\eta = \frac{\pi}{4} \zeta n^2 \int_0^{\infty} g(r) w^2(r) r^3 dr. \quad \text{(B.2)}}$$

If w^2 decreases fast (but smoothly) and the particles are hard and dense enough, so that $g(r)$ exhibits a sharp peak at $r = a_0$, the viscosity in Eq. B.2 can be further approximated as

$$\begin{aligned}
\eta &\simeq \frac{1}{8} \zeta n (2\pi n) \int_{a_0 - \epsilon}^{a_0 + \epsilon} g(r) w^2(r) r^3 dr. \\
&\simeq \frac{\zeta n w^2(a_0)}{8} (2\pi n) \int_{a_0 - \epsilon}^{a_0 + \epsilon} g(r) r^3 dr \\
&\simeq \frac{1}{8} \zeta n w^2(a_0) a_0^2 z_c,
\end{aligned}$$

where z_c is the coordination number, *i.e.*, the number of first neighbours (at a distance $r \sim a_0$).

Equation B.2 is valid for a one-component system, but the extension to binary mixtures, of components A and B, is straightforward; with transparent notations, the viscosity reads

$$\eta = \frac{\pi}{4}\zeta \int_0^\infty \left[n_A^2 g_{AA}(r) + 2n_A n_B g_{AB}(r) + n_B^2 g_{BB}(r)\right] w^2(r)\, r^3 dr. \quad \text{(B.3)}$$

In the considered Lennard-Jones system, this leads to $\eta = 0.726\,\zeta$.

AppendixC. Determination of the local stiffness tensors

With our condensed notations for the stress and strain tensors (Eq. 6), the macroscopic stiffness tensor of an isotropic material of bulk modulus K and shear modulus μ reads

$$\mathbf{C} = \begin{pmatrix} K+\mu & K-\mu & 0 \\ K-\mu & K+\mu & 0 \\ 0 & 0 & 2\mu \end{pmatrix}.$$

In comparison, local stiffness tensors display rather unusual properties. To grasp the meaning of their (lack of) symmetries, some brief general considerations about elasticity and deformation are in order.

Suppose that a small macroscopic strain $\bar{\boldsymbol{\epsilon}}$ is applied to a sample and focus on a mesoscopic region $\mathcal{S}$. The local linear strain tensor $\boldsymbol{\epsilon}$ is defined as the *symmetric* tensor that best matches the displacements of the particles in $\mathcal{S}$ due to the applied strain. Only if the deformation is strictly affine over the whole sample do the local strain tensors equate to $\bar{\boldsymbol{\epsilon}}$.

Because, for a given short-range interparticle potential, the local stress $\boldsymbol{\sigma}$ results from the local configuration of particles, it is reasonable (but not strictly necessary) to suppose the existence of a function f such that

$$\boldsymbol{\sigma} = f(\boldsymbol{\epsilon}).$$

Let us write the first-order Taylor expansion of f, provided that it exists,

$$\sigma_{\alpha\beta} - \sigma^{(0)}_{\alpha\beta} = C_{\alpha\beta\gamma\delta}\epsilon_{\gamma\delta} + \mathcal{O}\left(\|\boldsymbol{\epsilon}\|^2\right), \quad \text{(C.1)}$$

where α, $\beta \in \{x, y\}$ and $\sigma^{(0)}_{\alpha\beta}$ is the quenched stress in the original configuration. With condensed notations, Eq. C.1 turns into [5]

$$\begin{pmatrix} \sigma_{xx} \\ \sigma_{yy} \\ \sqrt{2}\sigma_{xy} \end{pmatrix} = \underbrace{\begin{pmatrix} C_{xx,xx} & C_{xx,yy} & C_{xx,xy} \\ C_{yy,xx} & C_{yy,yy} & C_{yy,xy} \\ C_{xy,xx} & C_{xy,yy} & C_{xy,xy} \end{pmatrix}}_{\mathbf{C}} \begin{pmatrix} \epsilon_{xx} \\ \epsilon_{yy} \\ \sqrt{2}\epsilon_{xy} \end{pmatrix} + \mathcal{O}\left(\|\boldsymbol{\epsilon}\|^2\right). \quad \text{(C.2)}$$

The affine strain-local stress approximation consists in replacing the components of $\boldsymbol{\epsilon}$ on the rhs of Eq. C.2 with those of the affine strain $\bar{\boldsymbol{\epsilon}}$, in order to

5. As a minor technical detail, note that, because the tensorial multiplication $C_{\alpha\beta\gamma\delta}\epsilon_{\gamma\delta}$ involves a summation on both ϵ_{xy} and ϵ_{yx}, components $C_{\alpha\beta,\gamma\delta}$ of the *second-rank* tensor $\mathbf{C}$ may not exactly equate to their counterparts in the *fourth-rank* tensor $C_{\alpha\beta\gamma\delta}$; for instance, $C_{xy,xy} = 2C_{xyxy}$.

determine $\mathbf{C}$ more easily. For subregions of size larger than $5\sigma_{AA}$, Mizuno et al. (2013) showed that this approximation is quite reasonable, although it slightly underestimates the spatial fluctuations of the elastic constants. On the other hand, should the local stress on the lhs be computed for a *local* deformation equal to $\bar{\boldsymbol{\epsilon}}$, *i.e.*, should the system not be allowed to relax to the energy minimum after the application of the affine strain $\bar{\boldsymbol{\epsilon}}$, then we would obtain the so-called Born term $\mathbf{C}^B$, which largely overestimates the stiffness of the disordered material (Mizuno et al., 2013).

For the time being, all components of the second-rank stiffness tensor $\mathbf{C}$ are independent. But, if the local stress derives from a (twice differentiable) local strain-energy density e, *i.e.*,

$$\sigma_{\alpha\beta} \equiv \frac{\partial e}{\partial \epsilon_{\alpha\beta}},$$

then

$$C_{\alpha\beta\gamma\delta} = \frac{\partial^2 e}{\partial \epsilon_{\alpha\beta} \partial \epsilon_{\gamma\delta}}.$$

It immediately follows that $C_{\alpha\beta\gamma\delta} = C_{\gamma\delta\alpha\beta}$; this symmetry property is transferred to the second-rank tensor $\mathbf{C}$ (thanks to the carefully chosen $\sqrt{2}$ prefactors in Eq. C.2). Indeed, Tsamados et al. (2009) observed numerically that, for coarse-graining regions larger than 5 Lennard-Jones particles in diameter, assuming a symmetric stiffness matrix $\mathbf{C}$ creates an error of less than 1% on the local stress evaluations. In the MD system under consideration, we quantify the asymmetry of the mesoscopic stiffness matrices, computed over regions of size $a = 5\sigma_{AA}$, with the following measure:

$$\|\Delta\mathbf{C}\| \equiv \sqrt{\sum_{\substack{i,j \in \\ \{xx,yy,xy\}}} \Delta C_{i,j}^2} \text{ with } \Delta\mathbf{C} \equiv \mathbf{C} - \frac{\mathbf{C} + \mathbf{C}^\top}{2}.$$

What should $\|\Delta\mathbf{C}\|$ be compared with? At first sight, the answer would be $\|\mathbf{C}\|$, but the latter is dominated by large symmetric terms involving the bulk modulus $K \approx 100$. Thus, on second thoughts, it appears more informative to remove the terms involving K; $\|\Delta\mathbf{C}\|$ should then be compared to, *e.g.*, $\langle \mathrm{Tr}\,(\mathbf{C}) - 2K \rangle = 4\,\langle \mu \rangle$, with $\langle \mu \rangle = 18.8$. From the histogram of $\|\Delta\mathbf{C}\|$ values plotted in Fig. C.9a, it transpires that deviations from symmetry in $\mathbf{C}$ are not strictly negligible, but symmetry may nevertheless be a decent *approximation*.

To further reduce the number of local parameters, the isotropic contraction/dilation vector $(\sqrt{2}/2\ \sqrt{2}/2\ 0)^\top$ is supposed to produce an isotropic compression and, thus, to be an eigenvector of $\mathbf{C}$, *ergo*

$$\begin{cases} C_{xy,xx} &= -C_{xy,yy} \\ C_{xx,xx} &= C_{yy,yy} \end{cases}$$

The assumptions of tensorial symmetry and isotropic response to contraction come down to projecting $\mathbf{C}$ onto a matrix of the form

$$\mathbf{C}' = \begin{pmatrix} \alpha & \delta & \beta \\ \delta & \alpha & -\beta \\ \beta & -\beta & \upsilon \end{pmatrix} \text{ with } \alpha, \delta, \beta, \upsilon \in \mathbb{R}, \tag{C.3}$$

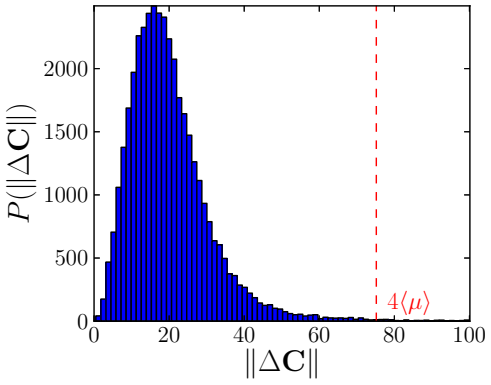

(a) Asymmetry.

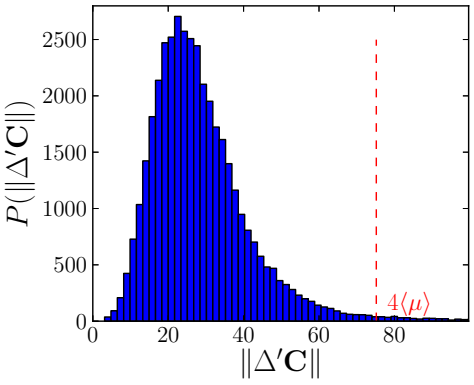

(b) Discrepancy with the matrix $\mathbf{C}'$ given in Eq. C.3.

Figure C.9: Histograms of the approximation errors made when supposing that the local stiffness tensors $\mathbf{C}$ are (a) symmetric, (b) of the form given in Eq. C.3.

where α and β will be the averages of the pairs $(C_{xx,xx}, C_{yy,yy})$ and $(C_{xy,xx}, -C_{xy,yy})$, respectively. The approximation error, quantified by $\|\Delta'\mathbf{C}\| \equiv \|\mathbf{C} - \mathbf{C}'\|$, is plotted in Fig. C.9b. As expected, the deviations are somewhat larger than were $\mathbf{C}$ only symmetrised, but they remain under control.

For each matrix $\mathbf{C}'$, we compute the eigenvalues $c_1 \leqslant c_2 \leqslant c_3$ and define:
- the small local shear modulus $\mu_1 \equiv c_1/2$,
- the large local shear modulus $\mu_2 \equiv c_2/2$,
- and the bulk modulus is $K \equiv c_3/2$.

The distributions of these local elastic constants are presented in Fig. C.10 and their mean values and standard deviations are summarised in Table 1. It should be noted that the average eigenvalues of the projected tensor $\mathbf{C}'$ differ by 10% or less from the eigenvalues of the full local stiffness tensors $\mathbf{C}$.

The components of $\mathbf{C}'$ can then be rewritten as follows

$$\begin{cases} \alpha & \equiv K + \mu_2 \cos^2 2\theta + \mu_1 \sin^2 2\theta \\ \delta & \equiv K - \mu_2 \cos^2 2\theta - \mu_1 \sin^2 2\theta \\ \beta & \equiv \frac{\sin 4\theta}{\sqrt{2}} (\mu_2 - \mu_1) \\ \upsilon & \equiv 2\mu_2 \sin^2 2\theta + 2\mu_1 \cos^2 2\theta \end{cases},$$

where the angle θ has been defined in Section 3.2.

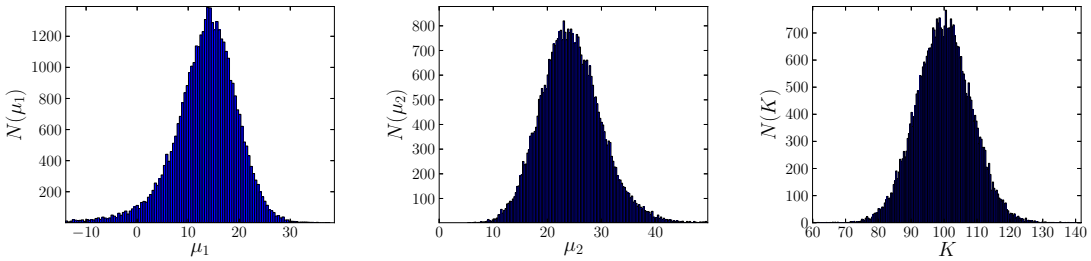

(a) μ_1 (b) μ_2 (c) K

Figure C.10: Histograms (number of counts) of the measured values of the local elastic constants μ_1, μ_2, and K in subregions of size $5\sigma_{AA} \times 5\sigma_{AA}$ in the MD system.